Journal of Medical Robotics Research, Vol. 2, No. 4 (2017) 1750006 (13 pages)

DOI: 10.1142/S2424905X17500064

Journal of Medical Robotics Research
http://www.worldscientific.com/worldscinet/jmrr

Journal of Medical Robotics Research

The MIRIAM Robot: A Novel Robotic System for MR-Guided Needle Insertion in the Prostate

Pedro Moreira[*,**], Gert van de Steeg[*], Thijs Krabben[†], Jonathan Zandman[†], Edsko E. G. Hekman[*], Ferdinand van der Heijden[‡], Ronald Borra[§,¶], Sarthak Misra[*,‖]

[*]*Surgical Robotics Laboratory, Department of Biomechanical Engineering University of Twente, The Netherlands*

[†]*DEMCON Advanced Mechatronics BV, The Netherlands*

[‡]*Robotics and Mechatronics, University of Twente, The Netherlands*

[§]*Faculty of Medical Sciences, Department of Nuclear Medicine and Molecular Imaging University of Groningen and University Medical Center Groningen, The Netherlands*

[¶]*Medical Imaging Centre of Southwest Finland, Department of Diagnostic Radiology Turku University Hospital, Turku, Finland*

[‖]*Surgical Robotics Laboratory, Department of Biomedical Engineering, University of Groningen and University Medical Center Groningen, The Netherlands*

Early prostate cancer detection and treatment are of major importance to reduce mortality rate. magnetic resonance (MR) imaging provides images of the prostate where an early stage lesion can be visualized. The use of robotic systems for MR-guided interventions in the prostate allows us to improve the clinical outcomes of procedures such as biopsy and brachytherapy. This work presents a novel MR-conditional robot for prostate interventions. The minimally invasive robotics in an magnetic resonance imaging environment (MIRIAM) robot has 9 degrees-of-freedom (DoF) used to steer and fire a biopsy needle. The needle guide is positioned against the perineum by a 5 DoF parallel robot driven by piezoelectric motors. A 4 DoF needle driver inserts, rotates and fires the needle during the procedure. Piezoelectric motors are used to insert and rotate the needle, while pneumatic actuation is used to fire the needle. The MR-conditional design of the robot and the needle insertion controller are presented. MR compatibility tests using T2 imaging protocol are performed showing a SNR reduction of 25% when the robot is operational within the MR scanner. Experiments inserting a biopsy needle toward a physical target resulted in an average targeting error of 1.84 mm. Our study presents a novel MR-conditional robot and demonstrated the ability to perform MR-guided needle-based interventions in soft-tissue phantoms. Moreover, the image distortion analysis indicates that no visible image deterioration is induced by the robot.

Keywords: MR-conditional robots; needle-based interventions; MR-guided needle steering; prostate biopsy; prostate interventions.

1. Introduction

Malignant tumors in the prostate are the most frequent type and are the second leading cause of death from cancer among men [1]. In order to decrease the mortality rate, early detection and treatment are of major importance. Therefore, efficient techniques for diagnosing and

Received 7 April 2016; Revised 7 July 2016; Accepted 12 August 2016; Published 11 October 2016. This paper was recommended for publication in its revised form by Editor Dan Stoianovici.
Email Addresses: ***p.lopesdafrotamoreira@utwente.nl*

treating prostate cancer are essential. The most common clinical method for prostate cancer diagnosis is the transrectal ultrasound (TRUS)-guided biopsy, where a needle is inserted into the prostate to collect tissue samples for a clinical analysis. TRUS-guided biopsy has a cancer detection rate of only 40% [2]. An early stage tumor in the prostate is usually an isoechoic lesion and cannot be visualized in ultrasound images. Magnetic resonance (MR) imaging offers an enhanced visualization of the prostate, in which an early stage lesion can be localized. MR-targeted biopsy with fusion of MR and TRUS imaging is a promising practice and can present better results when compared to traditional TRUS-guided prostate biopsy, but still requires further clinical validation [3–5]. On the other hand, MR-guided prostate biopsy offers the possibility of a more precise targeting than TRUS-guided with less needle insertions [2,6]. However, MR-guided interventions face several challenges, such as space constraints and electromagnetic (EM) compatibility of all devices located in the MR scanner room.

One of the most common guideline currently in use in Europe for MR-guided prostate biopsy requires manual alignment of the needle guide toward the suspected lesion [6–8]. The clinician places the needle guide in the patient's rectum. An MR imaging scan is performed and if the needle guide is not aligned toward the suspected lesion, the clinician manually repositions the needle guide. This procedure is repeated until the needle guide is correctly aligned. Manual alignment of the needle guide makes MR-guided prostate biopsy a time-consuming procedure [8]. Moreover, manual insertion of the needle does not allow correct deviations in the needle path due to tissue deformation and needle deflection. Needle deflection in MR-guided prostate biopsy is a major issue and the most significant cause of targeting error [9].

The current work presents a robotic system for transperineal prostate biopsy under MR guidance (Fig. 1). The transperineal approach is chosen due to the lower risk of sepsis and the possibility to access a greater proportion of peripheral zone in comparison with transrectal approach [10]. The proposed system has 9 degrees-of-freedom (DoF) capable of steering a biopsy needle toward the suspected lesion and removing tissue samples under the supervision of the clinician.

1.1. *Previous work*

Robots for MR environment have been the subject of a few state-of-the-art review papers [2,11]. In this section, we focus on robots devoted to needle-based interventions in the prostate. The simplest approach developed for MR-guided prostate biopsy uses a grid template to position the needle guide and orient the insertion [12,13]. However, these devices have limited accuracy and are difficult to operate due to the space constraints inside the MR scanner [3]. Several robotic systems were proposed to facilitate MR-guided prostate biopsy. These robotic systems can be differentiated into two main groups: (1) Systems with manually controlled needle insertion; (2) Systems with automated needle insertion. In the first group, the robot controls the position of the needle guide and the clinician manually inserts the needle. In the second group of robotic systems, the needle guide is robotically positioned and the robot inserts the needle.

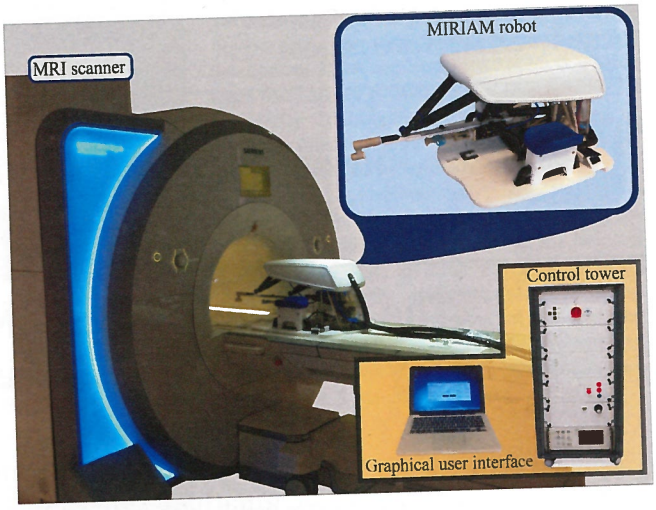

Fig. 1. Minimally invasive robotics in an magnetic resonance imaging environment (MIRIAM) robot is a 9 DoF MR-conditional system designed for needle-based interventions in the prostate. The system is capable of inserting, rotating and firing a biopsy needle to collect tissue samples. The user operates the robot from a graphical user interface within the control room. The control tower contains the motor drivers and the real-time controller which is also located in the control room. The pre-operative path planner and steering algorithm are integrated in the system to achieve a targeting error lower than 2.50 mm.

In the first group of robotic systems for prostate interventions, Schouten *et al.* developed a pneumatic positioning device for transrectal manually controlled prostate biopsy [8]. Stoianovici *et al.* presented a system for endorectal prostate biopsy composed of a passive arm and an actuated 3 DoF probe. The system was used to orient the needle guide using a pneumatic stepper motor [3]. The pneumatic stepper motor was developed to cope with problems stabilizing and overshoots inherent to pneumatic actuation [14]. The robot was tested both *in vitro* and in animal studies. Krieger *et al.* presented 2 DoF robotic system used to orient the needle guide and an endorectal probe for prostate interventions [15]. Tadakuma *et al.* proposed a parallel manipulator based on dielectric elastomer actuators to orient the needle guide during manual needle insertion into the prostate [16]. However, in these robotic systems, deviations from the intended needle path cannot be corrected,

since the needle is manually inserted. Moreover, manual insertion requires moving the patient out of the scanner bore to insert the needle, which is not required if an automated needle insertion is adopted.

In the second group of robots, Goldenberg *et al.* proposed a tele-operated MR-compatible robot for needle insertion with 5 DoF for transperineal prostate interventions [17]. The robot was actuated using non-magnetic motors and the user could manually control the insertion using a joystick. Van den Bosch *et al.* developed a robotic system for prostate seed implantation with automated needle insertion using pneumatic and hydraulic actuation [18]. Muntener *et al.* presented another robotic system for transperineal prostate seed implantation using pneumatic stepper motors [19]. The robot was tested in canine studies for prostate seed implantation and the average targeting error was 2.5 mm. Fischer *et al.* also proposed a pneumatic robot for prostate interventions with automated needle insertion [20]. Su *et al.* presented a robot with a similar architecture using piezoelectric motors [21]. The system had 5 DoF and was designed for general prostate interventions rather than a specific clinical application.

These previous studies with robotic systems for MR-guided prostate interventions were performed in open-loop and needle deflections were not taken into account. The work presented by Patel *et al.* is one of the few dealing with closed-loop needle steering [22]. However, the experiments were performed with a solid Nitinol wire and the focus of their study is on the needle tip tracking algorithm. Needle steering techniques can be used to correct the needle path in a closed-loop manner [23,24]. In this work, we adapt the techniques developed in our group for flexible bevel-tipped needles [25] to steer a clinically approved biopsy needle toward a target.

1.2. *Contributions*

This paper presents a novel 9 DoF robotic system for MR-guided transperineal prostate biopsy. The robot combines the high precision of piezoelectric actuation for needle placement and a pneumatic actuation to remove tissue samples. The system architecture and workflow are outlined by extensive clinical inputs. The system is able to perform fully automated prostate biopsies under clinical supervision. The multiple DoF of the robot allow us to position and orient the needle guide along the perineum. To the best of our knowledge, our work is the first one to integrate an MR-conditional robot, a preoperative planning, a needle tip tracking and a steering controller in order to compensate for undesired deviations due to needle deflection and tissue deformation. The current study aims to evaluate the overall functionality of a novel MR-conditional robot, such as MR-compatibility, steering capability, needle insertion accuracy and tissue removal. MR-compatibility tests and needle steering into phantom tissues are presented to validate the proposed system.

2. Magnetic Resonance Conditional Robot Design

This section describes the system requirements defined for a robot-assisted transperineal prostate biopsy, the mechatronic design of the robot and the control architecture.

2.1. *System requirements*

The system requirements are defined based on clinical inputs and are divided into two main groups: robot workspace and needle insertion requirements.

- *Workspace* — The workspace is defined by the anthropometric data of a patient in semi-lithotomy position. The prostate is consider to have sizes around $40 \times 30 \times 30$ mm and center located at 70 ± 20 mm beneath the perineal skin [26]. The space between the patient legs and the prostate location are used to define the range of robot movement [27]. The summary of the workspace requirements are presented in Table 1.

Table 1. Workspace requirements for transperineal MR guided prostate biopsy.

Requirement	Range
Translation in x-direction (Fig. 2)	−12–12 mm
Translation in y-direction	50–120 mm
Translation in z-direction	0–50 mm
Rotation around vertical axis	−15–15°
Needle insertion	−30–150 mm
Needle rotation	∞

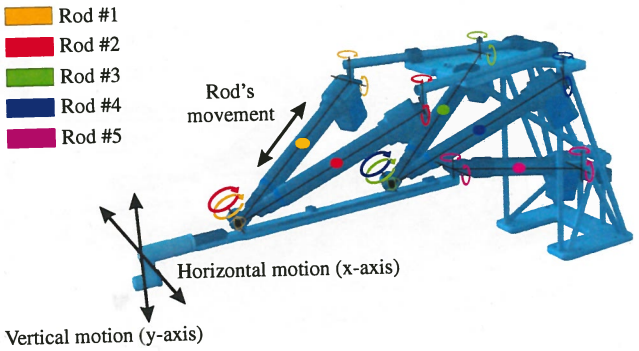

Fig. 2. The robot movement is provided by extending and retracting five rods. The extension and retraction of the rods allow the robot to move the needle along the Cartesian axis and rotate it around the vertical and horizontal axis.

ceramic driving disk. The needle can rotate along its own axis of insertion with a maximum speed of 160 RPM. An optical encoder (EM1, US Digital, Vancouver, USA) measures the needle rotation, which is important to steer the needle toward the target region. After the needle reaches the target region, the driver fires first the stylet and then the cannula to collect a tissue sample. Both the stylet and the cannula are fired by pneumatic actuators. Air-operated pneumatic valves (sys5440, SMC, Tokyo, Japan) pressurize the two cylinders of the needle driver (Fig. 3). The force exerted during the biopsy can be controlled by changing the air pressure of the pneumatic system in the control tower.

2.3. *Robot controller architecture*

The clinician supervises the robot operation through a GUI running on a computer inside the control room (Fig. 4). During the preoperative planning, the GUI allows the clinician to load and navigate via the MR images in order to define the target location. The preoperative images are also used to detect the fiducial located at the needle guide (Fig. 3) and define the robot position with respect to the patient coordinate frame. The clinician's commands are sent to the robot's low-level controller running on a computer equipped with a PCI-6602 counter card and a PCI-6713 analog output card (National Instruments, Austin, TX, USA) which is placed in the control tower. The control tower also contains the piezoelectric drivers (AB1A Driver Amplifier, Nanomotion, Yokneam, Israel). The flowchart with an overview of the robot controller architecture is presented in Fig. 5. The communication between the control tower and the robot is done through shielded electrical cables and pneumatic hoses (10 m long). The control tower is located in the control room to avoid EM interference in the MRI scanner.

3. Needle Insertion Control

In this section the method used to control the insertion of a clinically approved biopsy needle is presented. The

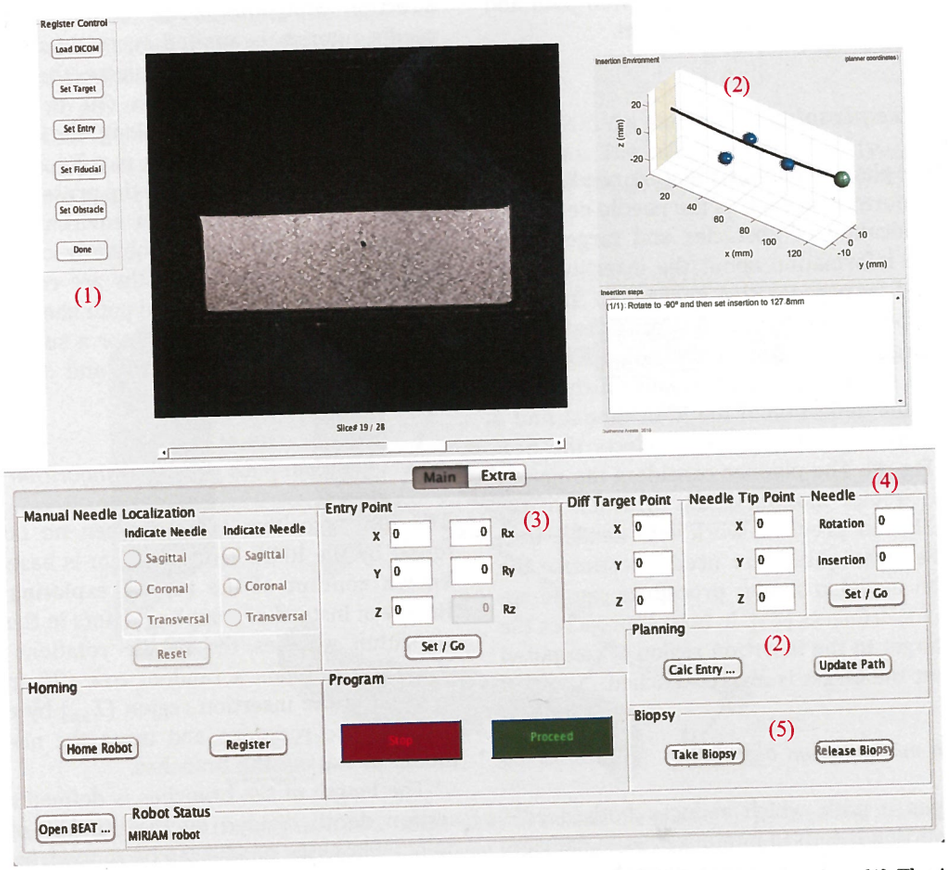

Fig. 4. The graphical user interface (GUI) used by the clinician to control the MIRIAM robot operation. (1) The interface used to navigate through the MR slices and define the obstacles and target location. This information is used to run the preoperative planner (2), which defines the best entry point. The user can supervise and control the needle entry position (3) and the needle insertion (4). When the needle reaches the target, the pneumatic actuation is used to collect the tissue sample (5).

- *Needle insertion requirements* — The insertion requirements are defined based on our prior experience with needle steering. The robot must insert the clinically approved biopsy needle (MR-Clear Bio-Cut, Sterylab, Milan, Italy) for MR-guided interventions. The maximum insertion velocity is set to be 20 mm/s with a maximum insertion force of 18 N [28]. The robot should be capable of rotating the needle during the insertion to correct for deviation from the intended path and achieve a targeting error lower than 2.50 mm. The maximum targeting error is determined based on the smallest clinically significant tumor in pathology (diameter of $\sim$ 5 mm) [29]. The tissue sample is collected by firing the biopsy needle. The robot must be able to generate a force of 30 N in order to cut the tissue sample.

2.2. *Robot design*

The development of the robotic system is divided into two main tasks: the parallel robot design and the needle driver design. The MIRIAM robot consists of a 5 DoF parallel robot to position and orient the needle guide (Fig. 3) and a 4 DoF needle driver to insert, rotate and fire the biopsy needle.

2.2.1. *Parallel robot*

The 5 DoF parallel robot contains 5 adjustable length rods which allow translations in the three Cartesian axes and two rotations (around x- and y-axis). Each rod is actuated by a nonmagnetic, piezoelectric motor (HR2, Nanomotion, Yokneam, Israel) which is radially mounted onto a ceramic driving wheel attached to a hard anodized aluminum spindle. Rod lengths are measured by optical incremental rotary encoders (EM1, US Digital, Vancouver, USA). The rods are attached to a static ceramic frame at one end and to the needle driver at the other end. The parts of the robot are constructed from plastics such as polyetheretherketone (PEEK), polyoxymethylene (POM), nylon, acrylic glass and Iglidur. The parts of the robot that require high stiffness are constructed from carbon filled PEEK and carbon reinforced tubes, such as housings for the piezoelectric motors and the rods, respectively. The robot frame is constructed of light-weight ceramic bars. Together with ceramic plates, these bars form a one-piece glued assembly which is protected by 3D printed covers (Fig. 3). The design of the parallel structure allows the robot to move within the workspace specified in Sec. 2.1. In addition, the robot is also able to rotate around x-axis (horizontal axis) between $-5°$ and $15°$. Moreover, the maximum range of the reachable needle tip workspace in the x-axis is 74 mm and 103 mm in the y-axis. *Please refer to the accompanying video that demonstrates the robot motions.* This workspace guarantees that the robot is able to place the needle guide along the entire perineum in the required pose and reach the entire prostate even considering significant variation in prostate size and location. The needle guide contains a fiducial marker to locate the robot with respect to the coordinate frame of the MR scanner. Moreover, there are three pins under the robot base that fit onto the MR table and lock the base of the robot. Therefore, the robot is always aligned with the coordinate frame of the MR scanner. It is important to mention that the needle guide can be detached from the robot to be sterilized. A surgical drape can also be used to protect the robot and meet the sterilization requirements.

2.2.2. *Needle driver*

The needle driver inserts, rotates and fires the biopsy needle. The insertion is achieved by a piezoelectric motor (HR8, Nanomotion, Yokneam, Israel) mounted onto a ceramic stage (Fig. 3). The maximum insertion depth is 150 mm, which is measured by a reflective optical encoder (LIK41, Numerik Jena, Jena, Germany). The needle rotation is provided by another piezoelectric motor (HR1, Nanomotion, Yokneam, Israel) axially mounted in a

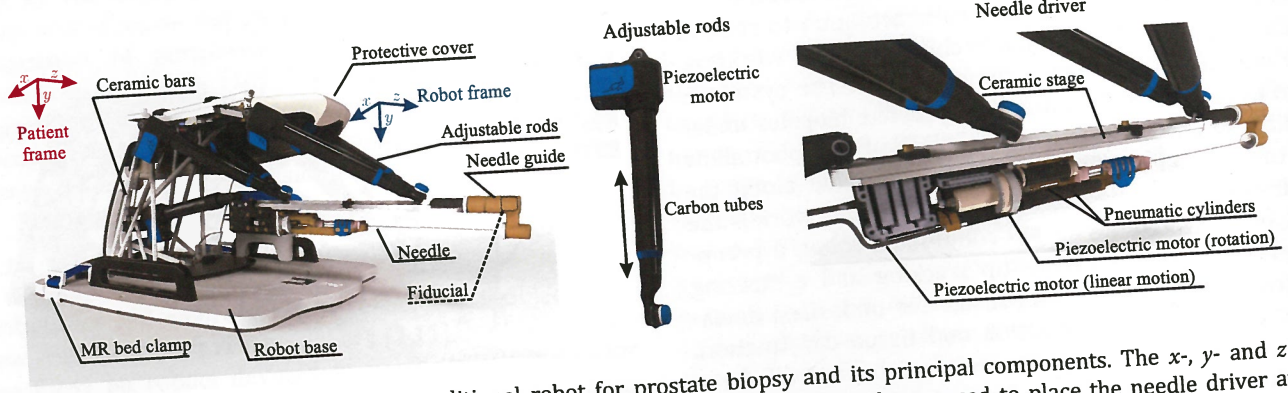

Fig. 3. The left image shows the MR-conditional robot for prostate biopsy and its principal components. The x-, y- and z-axis correspond to the Axial, Coronal and Sagittal planes, respectively. The adjustable rods are used to place the needle driver at the correct insertion location. The needle driver inserts and rotates the needle using piezoelectric motors, and fires the needle using pneumatic actuation.

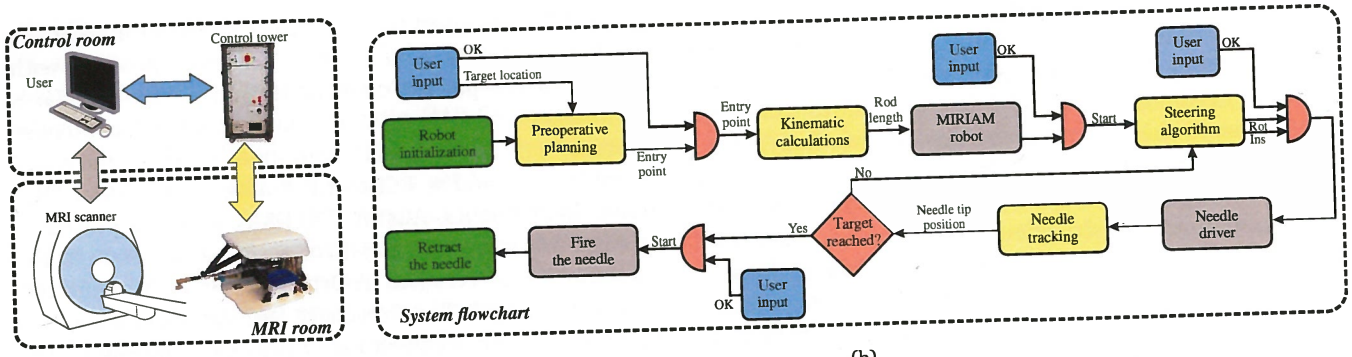

Fig. 5. (a) The user supervises the MIRIAM robot operation through a GUI inside the control room. The user commands are sent to the Real-Time Simulink PC located in the control tower. The communication between the control tower and the robot is done through shielded cables. (b) During the robot initialization, the zero position of all motors and the position of the robot in the patient coordinate frame are detected. The preoperative planner uses the target location selected by the user to define the needle entry point. The information about the entry point is used to calculate the desired length of each rod. The insertion starts after the robot places the needle driver in the correct entry point. The steering algorithm defines the needle rotation (Rot) and insertion step (Ins). The needle tip is tracked and the operation repeats until the target is reached. The needle is fired when the tip reaches the target location. For safety reasons, the clinician supervises the entire operation and can abort the procedure at any time.

preoperative planning used to define the needle entry point is presented. This is followed by the steering controller used to keep the needle on the desired path and the MR-based needle tip tracking algorithm.

3.1. *Preoperative planning*

The preoperative planner defines the best needle entry point based on information such as the needle deflection model and the location of obstacles and targets. The planner uses the information about the insertion environment provided by preoperative images. An insertion environment is constituted by: (1) Insertion region; (2) Obstacles; (3) Targets. A rotation minimization algorithm (RMA) calculates the shortest path based on the kinematics of the needle deflection. If the RMA cannot find a path, a random path generator (RPG) selects the best possible path (Fig. 4). The planner considers the needle deflection as a circular motion in the direction of the bevel tip angle. In our previous work with flexible needles noninvasive techniques were used to estimate the needle deflection model, a similar procedure can be applied for *in vivo* experiments [25]. In both approaches the path from the target to the insertion region is computed to guarantee that the target is always reached.

3.1.1. *Rotation minimization algorithm*

The RMA defines a path which reduces both needle rotation and insertion length to minimize tissue damage. The algorithm defines a path direction along the minimal distance (d) connecting the insertion region ($\mathcal{I}_{\text{ins}}$) and the target ($\mathbf{T}_{\text{tar}} \in \text{SE}(3)$). In the current implementation, the path direction is on a plane parallel to the xz-plane, since robot rotations about the horizontal axis have been restrained. The needle path is computed along the path direction using the needle deflection model. An axial needle rotation is applied every time a semi-circumference is completed to minimize the total amount of rotation. The planned path ($\mathbf{P}$) is then represented by a sequence of points along the needle path, such as $\mathbf{P} = [\mathbf{p}_1, \mathbf{p}_2, \ldots, \mathbf{p}_i]$ where $\mathbf{p}_i \in \mathbb{R}^3$ are the coordinates of each point on the path. In the presence of obstacles or no-go zones in the insertion environment, the planned path has to be checked for obstacle collisions. If a collision occurs, sub-optimal paths are computed by incrementally rotating the original path about the z-axis. If the RMA cannot find an optimal nor a sub-optimal solution that respects robot constraints and obstacle avoidance, the RPG algorithm is used.

3.1.2. *Random path generator algorithm*

The RPG algorithm is used when no possible path is found by the RMA. The algorithm is based on the well-known concept of the rapidly exploring random tree. However, instead of sampling points in the 3D space, our algorithm samples the needle rotations (inputs). The algorithm expands a random tree ($\mathcal{T}$) from the target location to the insertion region ($\mathcal{I}_{\text{ins}}$) by randomly sampling needle rotations and using the needle deflection model to expand the branches.

The length of the branches is defined as the total insertion depth divided by the number of intermediate points where the needle can be rotated. In order to avoid excessive needle rotations, a probability ($\mathfrak{p}$) of needle rotation is defined at the end of each branch. In this work, $\mathfrak{p}$ is set to 10%. Increasing the probability of rotation will result in a higher path viability, but it will

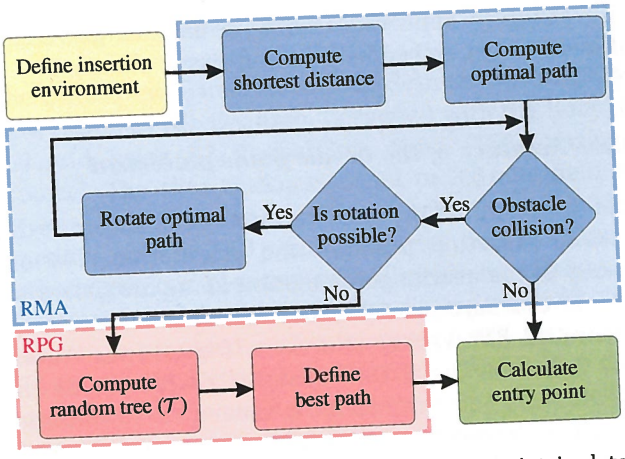

Fig. 6. Flowchart of the RMA. The insertion point is determined by computing the shortest linear path between the target and the insertion region. The needle deflection model is used to create the needle path (optimal path). If a collision occurs the path is rotated about its own direction and about the z-axis. The process is repeated iteratively and the shortest path is chosen. If the algorithm is not able to choose a path or if the chosen path violates the robot constraints, the RPG is used.

also raise the total number of rotations. The explored tree ($\mathcal{T}$) is composed of at least 3000 candidate paths. A path is considered a candidate if it crosses the insertion region ($\mathcal{I}_{\text{ins}}$) and if no obstacle collision occurs. The path with less amount of needle rotation is extracted from the tree and the insertion point and angle are calculated. The planned path ($\mathbf{P}$) is a sequence of Cartesian points ($\mathbf{p}_i$), which are used by the needle steering control to reach the target.

3.2. *MR image-based needle tracking*

During the procedure, the needle insertion is divided in iterative steps. At the end of each iteration an MR scan is performed. Our tracking system processes MR images and estimates the needle tip position and orientation. The image dataset of axial slices is loaded to the GUI and displayed on the screen. The resulting images provide a radial cross-sectional view of the needle, which has a circular shape. The user selects the last MR image slice with a visible cross-sectional view of the needle, corresponding to the needle tip (Fig. 7). A series of image processing techniques, such as adaptive histogram equalization and thresholding, are used to determine the centroid of the cross-section view, which is defined as the needle tip position ($\mathbf{p}_{\text{tip}} \in \mathbb{R}^3$). The tracking algorithm estimates the needle tip orientation using a vector ($\mathbf{m} \in \mathbb{R}^3$) defined by the difference between needle tip position ($\mathbf{p}_{\text{tip}}$) and a needle shaft point ($\mathbf{p}_{\text{shaft}} \in \mathbb{R}^3$) as

$$\mathbf{m} = \begin{bmatrix} \Delta x \\ \Delta y \\ \Delta z \end{bmatrix} = \mathbf{p}_{\text{tip}} - \mathbf{p}_{\text{shaft}},$$

where Δx, Δy and Δz are the coordinates in the Cartesian axes. The needle shaft point ($\mathbf{p}_{\text{shaft}}$) is determined from the image slice located 3 mm behind the needle tip

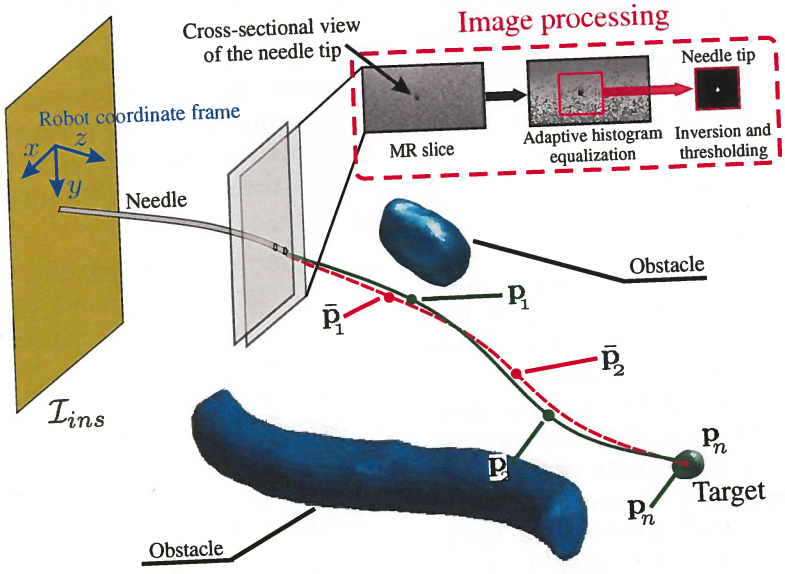

Fig. 7. The MR image based needle tracking uses axial image slices to localize the needle tip position and orientation. The images provide a cross-sectional view of the needle and a series of image processing techniques are used to estimate the centroid of the needle tip. The needle orientation is estimated also using the position of the needle shaft in the slice 3 mm behind the needle tip. The steering algorithms uses the needle tip position, orientation and a needle deflection model to calculate the next path points ($\mathbf{p}$) where the needle should be rotated. A cost function based on the path points ($\mathbf{p}$, $\mathbf{p}_2$,...,$\mathbf{p}_n$) and the pre-planned path points ($\bar{\mathbf{p}}_1$, $\bar{\mathbf{p}}_2$, ..., $\bar{\mathbf{p}}_n$) is used to define the best possible path and the sequence of needle rotations.

(Fig. 7). The in-plane accuracy is ± 0.25 mm, which results in an orientation error of $\pm 4.8°$. The needle orientation is given by the rotations around the Cartesian coordinate frame. The rotation around the x-axis (θ) and around the y-axis (ϕ) are computed by

$$\theta \approx \tan^{-1}\frac{\Delta z}{\Delta y} \quad \text{and} \quad \phi \approx \tan^{-1}\frac{\Delta x}{\Delta z}. \tag{1}$$

The needle tip rotation about the z-axis is determined from the needle rotation motor. The estimated needle tip position and orientation are used by the steering algorithm to correct the needle path during the insertion.

3.3. *Needle steering controller*

Needles with asymmetric bevel tips naturally bend when inserted into soft tissues. This bending effect is used to steer the needle toward a target by applying axial rotations. In our previous work, needle rotations were applied every second to align the bevel tip toward the target during ultrasound-guided needle steering [25]. In MR-guided needle, steering this technique might not work properly since the image acquisition rate is at least 20 times lower than ultrasound. A needle steering controller that only aligns the bevel tip toward the next path point can result in unreachable subsequent path points. Therefore, the needle rotation should be computed taking into account all path points ahead of the current needle tip (Fig. 7). The controller computes thousands of paths from the current needle tip ($\mathbf{p}_{\text{tip}}$) until the target location. The sequence of needle rotations that minimizes a cost function ($\mathbf{J}$) is chosen. In this work, the cost function is defined to guarantee that the needle will follow the pre-planned path and reduce the final targeting error. The cost function is defined as

$$\mathbf{J} = K_f|\bar{\mathbf{p}}_n - \mathbf{p}_n| + \sum_{i=1}^{n-1}|\bar{\mathbf{p}}_i - \mathbf{p}_i|, \tag{2}$$

where $\bar{\mathbf{p}}_i \in \mathbb{R}^3$ are the pre-planned path points, $\mathbf{p}_i \in \mathbb{R}^3$ are the path points defined by the steering algorithm, i is the path point index, n is the total number of path points from the current needle tip location to the target and K_f is a weighting factor for the final targeting error, which is set to 4 in this work. The algorithm is used to steer the needle during MR-guided steering experiments.

4. Experimental Results

In this section, we first assess the accuracy of the needle guide placement. We also present the MR-compatibility evaluation and the needle steering experiments. The clinically approved needle is inserted toward a physical target embedded in a soft-tissue phantom.

4.1. *Accuracy of the needle guide placement*

The needle guide is placed against the phantom at the desired insertion position and orientation. The accuracy of the needle guide motion along the Cartesian axis is evaluated outside the MR scanner using an Aurora v2 EM tracker (Northern Digital Inc., Waterloo, Canada). The 6 DoF probe is placed inside the needle guide and the robot is moved to 20 different positions along the workspace. The robot motion is calculated by the difference between the final robot position and the initial robot position, both measured using the EM tracker. The initial and final robot positions are computed by the average of 100 samples.

The mean error and the standard deviation along the x-axis is 0.14 ± 0.12 mm (Fig. 2). Along the y- and z-axis the mean errors and their standard deviations are respectively 0.17 ± 0.14 mm and 0.04 ± 0.50 mm. The errors in the rotations about the x-, y- and z-axis are 0.011 ± 0.021, 0.021 ± 0.001 and 0.032 ± 0.044 rad, respectively. It is important to notice that the motion errors are lower than the accuracy of the EM tracker, which shows that the robot positioning error is lower than the accuracy of the system.

4.2. *MR compatibility evaluation*

The MIRIAM robot is intended to work in the MR environment, thus MR compatibility tests are important to validate the robot design. The standard F2503-05 of the American Society of Testing and Materials (ASTM) defines the following three types of MR compatibility labels [3]:

- *MR-Safe*: A system that poses no known physical risks in all MR environments. This label can only be achieved if the system has no electrical actuation nor metallic parts.
- *MR-Conditional*: A system that has been demonstrated to pose no known hazards in a specified MR environment with specified conditions of use.
- *MR-Unsafe*: A system that is known to pose hazards in the MR environment.

The design of the MIRIAM robot uses piezoelectric motors and encoders in order to achieve precise motions. Therefore, the robot is labeled as *MR-Conditional*. An important aspect of MR compatibility is the amount of image degradation caused by the robot. An analysis based on SNR is used to quantify the amount of noise induced by the robot in MR images.

4.2.1. *Signal-to-noise ratio analysis*

The SNR is evaluated in an MRI Scanner MAGNETOM Aera (Siemens AG, Erlangen, Germany) with the Body18 coil and using T2 Turbo Spin Echo (TSE) imaging protocol. The slice thickness is set to 3.0 mm, field of view (FoV) of 200 mm × 200 mm, echo time of 1.01 s, repetition time of 7.50 s and acquisition time of 4.5 min. An homogeneous phantom with dimensions 160 mm × 160 mm is used in the SNR analysis experiments. The phantom is prepared with a mixture of 85% water and 15% gelatin (Dr. Oetker, Ede, The Netherlands). The SNR is calculated as the mean pixel intensity of a region in the center of the phantom divided by the image noise outside the phantom. The noise outside the phantom is calculated as the average of pixel intensity in the four corners of the MR image divided by 1.25 [21]. The following configurations are used in the SNR evaluation:

(1) Baseline.
(2) Phantom and MIRIAM robot powered off.
(3) Phantom and MIRIAM robot powered on.
(4) Phantom and MIRIAM robot with the piezoelectric motors running.

In the last three configurations, the robot is placed with the needle guide in contact with the phantom edge. For each configuration the SNR is calculated in 25 coronal images. The results are presented in Fig. 8. The SNR drops 16% when the robot is placed inside the scanner and drops 25% when the robot power is turned on. In the last configuration, the SNR reduces 27% when the insertion and rotation motors are running. The robot architecture with the piezoelectric motors away from the needle guide (i.e., away from the imaging area) and the EM shielding resulted in a reduced level of induced noise. However, the SNR analysis alone cannot fully assess the image deterioration due to the presence of the robot inside the MRI scanner.

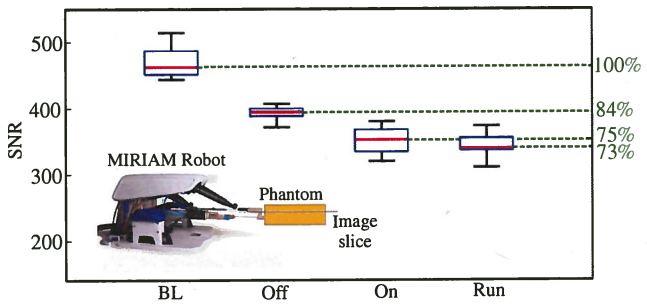

Fig. 8. The signal-to-noise ratio (SNR) analysis is presented. The SNR is calculated in four different configurations: Baseline (BL), robot powered off (Off), robot powered on (On) and robot running (Run). The red line is the median of the 25 SNR measurements, the edges of the blue box are the 25th and 75th percentiles. The error bars extend to the most extreme data points.

4.2.2. *Image distortion analysis*

In addition to the SNR analysis, the image distortion is also analyzed using a method based on a deterioration factor. The image deterioration factor defined by Stoianovici [30] is used to evaluate the image distortion due to the presence of the robot. The analysis is divided into one passive and two active tests. The three tests are defined as

- Passive test (P) — Represents the noise induced by the presence of the robot in the scanner. It is calculated based on the difference between: (a) images with the robot powered off and (b) images without the robot.
- Active test #1 ($A1$) — Represents the noise induced by powering the motors on. It is calculated based on the difference between: (a) images with the robot powered on and (b) images with the robot powered off.
- Active test #2 ($A2$) — Represents the noise induced by running the motors. It is calculated based on the difference between: (a) images with the motors running and (b) images with the robot powered on.

The deterioration factor for each axial image slice is calculated as

$$e^T(z) = \frac{100}{2^{2p_d}} \sum_{\substack{x=1 \\ y=1}}^{\substack{x=r_x \\ y=r_y}} \frac{(p^a_{xy} - p^b_{xy})^2}{r_x r_y} \quad \text{for } T \in \{P, A1, A2\}, \quad (3)$$

where p^a_{xy} and p^b_{xy} are the pixel intensity values of the two MR images for each test, p_d is the pixel depth, r_x and r_y are the image resolution values and z is the distance of the image slice to the robot.

The deterioration factor is calculated for the axial images of a gelatine phantom containing eight randomly-located spherical objects with diameters between 6 mm to 8 mm. The spherical objects are made of polyvinyl chloride (PVC) and the phantom has the same gelatine concentration as the one used in the SNR analysis. Axial images of the phantom are acquired using T2-TSE imaging protocol with a FoV of 160 mm by 160 mm, echo time of 1.5 s, repetition time of 8.50 s and the slice thickness is set to 1.0 mm.

The variations of the deterioration factors are plotted in Fig. 9. The deterioration factor reduces as the distance between the image slice and the robot increases. The total amount of interference induced by the robot is evaluated based on a global deterioration factor. The global deterioration factor is defined as the average values of the deterioration factor minus a baseline factor. When the passive global deterioration factor is lower than 2% and the active global deterioration factor is lower than 1%, the interference can be considered minimal or unobservable [30]. In our case, the deterioration factors are always lower than these limits, which

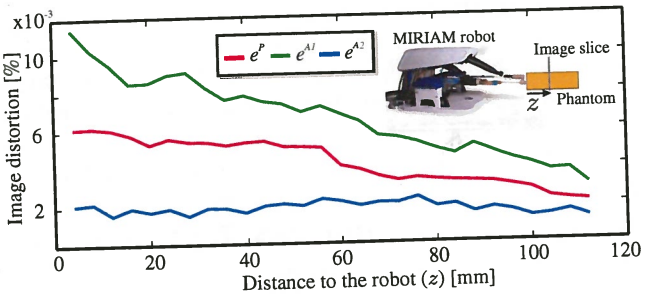

Fig. 9. The image deterioration factor for the three tests versus the distance between the images and the robot. The red line represents the passive test (e^P). The green line is the active test with the motors powered on but without motion (e^{A1}). While the blue line is the deterioration factor of the active test with the piezoelectric motors running (e^{A2}).

means that our system does not induce any interference perceivable by radiologists.

4.2.3. *Geometric distortion analysis*

The geometric distortion is defined by the NEMA standard MS 2-2008 as the maximum percent difference between measured distances in an image and the corresponding ground truth dimensions. A phantom containing 6 pins is prepared to evaluate the geometric distortion induced by the MIRIAM robot. The pins are made of Acrylonitrile Butadiene Styrene (ABS) and the distances between the pins are known. The pins are embedded in a phantom prepared with a mixture of 85% water and 15% gelatin (Dr. Oetker, Ede, The Netherlands). Each distance is measured in 24 different MR images and the average values are reported. The distances used in this analysis are illustrated in Fig. 10 and the percent differences are presented in Table 2. The maximum difference (0.82%) appears when the motors are running. These results show that the geometric distortion induced by the MIRIAM robot is negligible. Furthermore, the reduced amount of induced noise, image distortion and geometric distortion allow us to use the MR images as feedback to control the needle insertion.

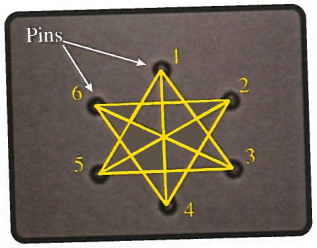

Fig. 10. Representative MR image used in the geometric distortion analysis. A set of 24 MR images of a gelatin phantom with six embedded pins are used to evaluate the geometric distortion. The yellow lines represent the measured distances.

Table 2. Geometric distortion evaluation: percent difference between the measured distances and ground truth.

	Baseline	Robot off	Robot on	Motors running
L_{1-4} [%]	0.30	0.05	0.05	0.15
L_{2-6} [%]	0.31	0.55	0.65	0.77
L_{3-5} [%]	0.37	0.77	0.70	0.67
L_{2-5} [%]	0.04	0.35	0.29	0.38
L_{2-4} [%]	0.58	0.49	0.82	0.82
L_{3-6} [%]	0.02	0.24	0.10	0.11
L_{3-1} [%]	0.55	0.02	0.47	0.55
L_{6-4} [%]	0.33	0.69	0.44	0.38
L_{1-5} [%]	0.38	0.11	0.02	0.02
Mean	0.31	0.36	0.78	0.42

4.3. *Needle steering experiments*

The targeting accuracy is evaluated in six needle insertions. A clinically approved 18-gauge biopsy needle (MR-Clear Bio-Cut, Sterylab, Milan, Italy) is inserted toward physical targets with 2 mm radius. The targets are made of PVC and embedded in a gelatin phantom prepared with a mixture of 85% water and 15% gelatin. Two phantoms are prepared, each one with three spherical obstacles and three targets. In transperineal prostate biopsy, the regions to be avoided by the needle are the urethra, anterior rectal wall and pelvic side wall. In the current experiments, spherical obstacles (diameter of 6 mm) are located halfway between the insertion region and the targets to demonstrate the ability of the system to handle obstacles. The target location varies as ($-39\,\text{mm} \leq x \leq 25\,\text{mm}$; $10\,\text{mm} \leq y \leq 19\,\text{mm}$; $110\,\text{mm} \leq z \leq 138\,\text{mm}$) (Fig. 11). The needle curvature is estimated in previous insertions and it is set to $1.5 \times 10^{-3}\,\text{mm}^{-1}$. The insertion step length is set to 15 mm. The robot initial position (i.e., the fiducial location with respect to the patient coordinate frame), the obstacle and the target locations are defined by the user using the preoperative images. The tracking algorithm uses the same T2-TSE imaging protocol as in Sec. 4.2.2. The results of the insertions performed in one soft-tissue phantom is presented in Fig. 11. The targeting error is defined as the Euclidean distance between the final needle tip position and the center of the target. The average targeting error is 1.86 mm with a standard deviation of 0.48 mm. This targeting error is three times lower than the average targeting error obtained by experienced clinicians in a phantom study reported by Blumenfeld *et al.* [9]. It is important to highlight that in all six experiments the targeting error is lower than the desired accuracy defined in Sec. 2.1. In addition, the time spent for each insertion is about 25 min, which is less than the time required for the conventional manual procedure currently being used in clinical practice and reported by

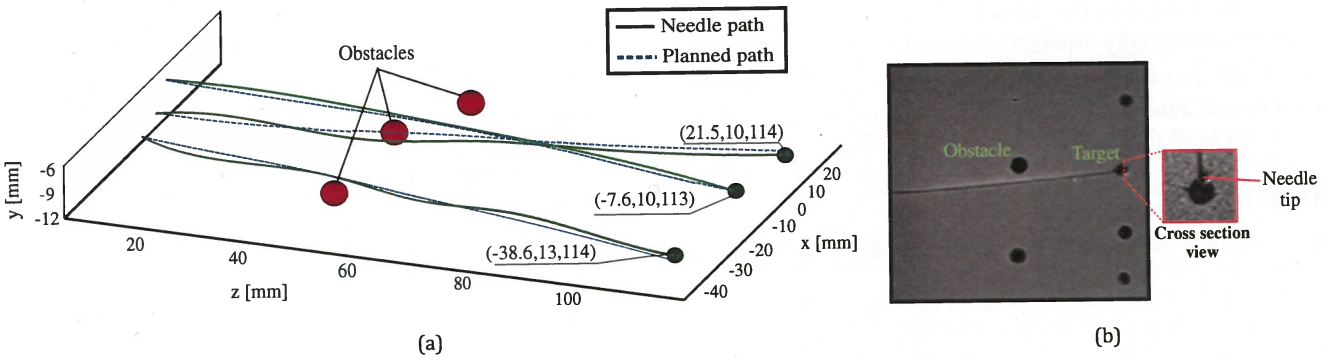

Fig. 11. Experimental results: (a) Representative results of steering a needle toward a physical target while avoiding physical obstacles. The green line is the needle path and the blue dash line is the preplanned path in three different insertions. (b) A coronal MR image of one representative insertion. The inset figure shows the cross-sectional view of the final needle tip position. *Please refer to the accompanying video that demonstrates the experimental results.*

Schouten *et al.* [8]. Furthermore, most of the insertion time is a result of performing MR imaging scans (3.6 min for each insertion step) and can be significantly reduced using a real-time imaging protocol.

4.4. *Tissue removal experiments*

The pneumatic actuation used to fire the biopsy needle is evaluated in *ex vivo* bovine tissues. The length of the removed tissue in five collected samples are measured. The average removed tissue length is 5.9 mm with a standard deviation of 1.3 mm. *Please refer to the accompanying video that demonstrates the experimental results.* It is important to notice that the length of tissue removed from *ex vivo* tissues is smaller than *in vivo* due to the lack of internal tissue pressure. Therefore, to assess the robot's capability of removing a tissue sample, the same experiment is performed using the Acecut needle gun (TSK Laboratory, Oisterwijk, Netherlands). An average tissue length of 5.6 mm with a standard deviation of 0.8 mm is obtained using the needle gun, which is similar to the results using the MIRIAM robot. A t-test between the two groups resulted in $p = 0.77$, which shows that there is no statistical difference between the two groups.

5. Conclusions

In this study, we present an MR-conditional robotic system for needle-based interventions in the prostate. The robot has 9 DoF and it is able to position the needle guide along the entire perineum using piezoelectric actuation. The natural bending effect of the needle when inserted into the tissue is used to steer it along a desired path. MR images are used by the needle tracking algorithm to estimate the needle tip position during the insertion. The needle rotation is calculated based on the needle tip position and the desired path. The MR-compatibility evaluation shows that the proposed system does not induce any significant artifacts in the image. In the worst scenario, with the piezoelectric motors running, the SNR drop is only 27%. The accuracy of the needle tip placement is tested in six insertions toward a physical target while avoiding obstacles. The needle steering experiments show an average targeting error of 1.84 mm. This accuracy is 0.66 mm less than the desired accuracy defined in the system requirements. Different aspects can impact the targeting accuracy, such as target motion and variations on the needle curvature. However, these factors can be mitigated by implementing a target tracking and an online curvature estimation.

Future work will focus on implementing a real-time MR imaging protocol. Such a protocol will allow us to drastically reduce the time spent during an insertion. The needle tracking algorithm will be improved for real-time MR imaging. Real-time MR images have lower SNR than T2 images, which makes the tip tracking a challenging task. One possible solution is to use the information from Sagittal and Coronal image slices to track the needle shaft [22]. We will also investigate a model-based needle tracking with the fusion of an adaptive needle deflection model and the real-time MR images. Moreover, with real-time imaging, an online curvature estimation will be implemented to handle nonhomogeneous tissues. A target tracking using MR images and deformable models will also be investigated. Additionally, it is planned to perform experiments in biological tissues and cadavers.

Acknowledgment

The authors would like to thank J. J. Füterrer and J. Heidkamp for their clinical insight during the design process of the MIRIAM robot. This research was supported by funds from the Dutch Ministry of Economic Affairs and the Provinces of Overijssel and Gelderland,

within the Pieken in de Delta (PIDON) Initiative, Project MIRIAM (Minimally Invasive Robotics In An MRI environment). Funding was also provided to RB by the Academy of Finland (130557,270352).

References

1. R. Siegel, D. Naishadham and A. Jemal, Cancer statistics, 2013, *CA: Cancer J. Clin.* **63**(1) (2013) 11–30.
2. J. J. Fütterer, S. Misra and K. J. Macura, MR imaging of the prostate: Potential role of robots, *Imaging Med.* **2**(5) (2010) 583–592.
3. D. Stoianovici, C. Kim, G. Srimathveeravalli, P. Sebrecht, D. Petrisor, J. Coleman, S. Solomon and H. Hricak, MRI-safe robot for endorectal prostate biopsy, *IEEE/ASME Trans. Mechatronics* **19**(4) (2014) 1289–1299.
4. G. Churukanti and M. M. Siddiqui, Prostate cancer: MRI-TRUS fusion biopsy versus 12-core systematic biopsy, *Nat. Rev. Urol.* **12** (2015) 369–371.
5. A. Peltier, F. Aoun, M. Lemort, F. Kwizera, M. Paesmans and R. V. Velthoven, MRI-targeted biopsies versus systematic transrectal ultrasound guided biopsies for the diagnosis of localized prostate cancer in biopsy naïve men, *Biomed. Res. Int.* **2015** (2015) 1–6.
6. J. O. Barentsz, J. Richenberg, R. Clements, P. Choyke, S. Verma, G. Villeirs, O. Rouviere and V. L. J. J. Fütterer, ESUR prostate MR guidelines 2012, *Eur. Radiol.* **12** (2012) 746–757.
7. D. Beyersdorff, A. Winkel, B. Hamm, S. Lenk, S. Loening and M. Taupitz, MR imaging-guided prostate biopsy with a closed mr unit at 1.5 t: Initial results, *Radiology* **2** (2005) 576–581.
8. M. G. Schouten, J. G. Bomers, D. Yakar, H. Huisman, E. Rothgang, D. Bosboom, T. W. Scheenen, S. Misra and J. J. Fütterer, Evaluation of a robotic technique for transrectal MRI-guided prostate biopsies, *Eur. Radiol.* **22**(2) (2012) 476–483.
9. P. Blumenfeld, N. Hata, S. DiMaio, K. Zou, S. Haker, G. Fichtinger and C. M. Tempany, Transperineal prostate biopsy under magnetic resonance image guidance: A needle placement accuracy study, *J. Magn. Reson. Imaging* **26**(3) (2007) 688–694.
10. P. Pepe and F. Aragona, Prostate biopsy: Results and advantages of the transperineal approach-twenty-year experience of a single center, *World J. Urology* **32**(2) (2014) 373–377.
11. H. Elhawary, Z. T. H. Tse, A. Hamed, M. Rea, B. L. Davies and M. U. Lamperth, The case for MR-compatible robotics: A review of the state of the art, *Int. J. Med. Robotics Comput. Assis. Surg.* **4**(2) (2008) 105–113.
12. S. Abdelaziz, L. Esteveny, P. Renaud, B. Bayle, L. Barbé, M. De Mathelin and A. Gangi, Design considerations for a novel MRI compatible manipulator for prostate cryoablation, *Int. J. Comput. Assis. Radiol. Surg.* **6**(6) (2011) 811–819.
13. J. Tokuda, K. Tuncali, I. Iordachita, S.-E. Song, A. Fedorov, S. Oguro, A. Lasso, F. M. Fennessy, C. M. Tempany and N. Hata, In-bore setup and software for 3t MRI-guided transperineal prostate biopsy, *Phys. Med. Biol.* **57**(18) (2012) 5823–5840.
14. D. Stoianovici, A. Patriciu, D. Petrisor, D. Mazilu and L. Kavoussi, A new type of motor: Pneumatic step motor, *IEEE/ASME Trans. Mechatronics* **12** (2007) 98–106.
15. A. Krieger, S.-E. Song, N. Cho, I. Iordachita, P. Guion, G. Fichtinger and L. Whitcomb, Development and evaluation of an actuated MRI-compatible robotic system for MRI-guided prostate intervention, *IEEE/ASME Trans. Mechatronics* **18** (2013) 273–284.
16. K. Tadakuma, L. DeVita, J. Plante, Y. Shaoze and S. Dubowsky, The experimental study of a precision parallel manipulator with binary actuation: With application to MRI cancer treatment, in *Proc. of the IEEE Int. Conf. on Robotics and Automation (ICRA)* (2008), pp. 2503–2508.
17. A. Goldenberg, J. Trachtenberg, W. Kucharczyk, Y. Yi, M. Haider, L. Ma, R. Weersink and C. Raoufi, Robot-assisted MRI-guided prostatic interventions, *Robotica* **28**(2) (2010) 215–234.
18. M. R. van den Bosch, M. R. Moman, M. van Vulpen, J. J. Battermann, E. Duiveman, L. J. van Schelven, H. de Leeuw, J. J. W. Lagendijk and M. A. Moerland, MRI-guided robotic system for transperineal prostate interventions: Proof of principle, *Phys. Med. Biol.* **55**(5) (2010) 133–140.
19. M. Muntener, A. Patriciu, D. Petrisor, M. Schar, D. Ursu, D. Y. Song and D. Stoianovici, Transperineal prostate intervention: Robot for fully automated MR imaging-system description and proof of principle in a canine model, *Radiology* **247**(2) (2008) 543–549.
20. G. Fischer, I. Iordachita, C. Csoma, J. Tokuda, S. DiMaio, C. Tempany, N. Hata and G. Fichtinger, MRI-compatible pneumatic robot for transperineal prostate needle placement, *IEEE/ASME Trans. Mechatronics* **13**(3) (2008) 295–305.
21. H. Su, W. Shang, G. Cole, G. Li, K. Harrington, A. Camilo, J. Tokuda, C. Tempany, N. Hata and G. Fischer, Piezoelectrically actuated robotic system for MRI-guided prostate percutaneous therapy, *IEEE/ASME Trans. Mechatronics* **20**(4) (2015) 1920–1932.
22. N. A. Patel, T. van Katwijk, G. Li, P. Moreira, W. Shang, S. Misra and G. S. Fischer, Closed-loop asymmetric-tip needle steering under continuous intraoperative mri guidance, in *Proc. IEEE Engineering in Medicine and Biology Society (EMBC)* (2015), pp. 4869–4874.
23. M. C. Bernardes, B. V. Adorno, P. Poignet and G. A. Borges, Robot-assisted automatic insertion of steerable needles with closed-loop imaging feedback and intraoperative trajectory replanning, *Mechatronics* **23**(6) (2013) 630–645.
24. N. A. Wood, K. Shahrour, M. C. Ost and C. N. Riviere, Needle steering system using duty-cycled rotation for percutaneous kidney access, in *Proc. of the Int. Conf. of the IEEE Engineering in Medicine and Biology Society (EMBC)*, Buenos Aires, Argentina (September 2010), pp. 5432–5435.
25. P. Moreira and S. Misra, Biomechanics-based curvature estimation for ultrasound-guided flexible needle steering in biological tissues, *Ann. Biomed. Eng.* **43**(8) (2014) 1716–1726.
26. D. Stoianovici, D. Song, D. Petrisor, D. Ursu, D. Mazilu, M. Muntener, M. Schar and A. Patriciu, MRI stealth robot for prostate interventions, *Minim. Invasive Ther. Allied Technol.* **16**(4) (2007) 241–248.
27. Y. Yu, T. Podder, Y. D. Zhang, W. S. Ng and V. Misic, Robot-assisted prostate brachytherapy, *Medical Image Computing and Computer-Assisted Intervention (MICCAI)* (2006), pp. 41–49.
28. T. Podder *et al.*, Effects of velocity modulation during surgical needle insertion, in *Proc. of the Int. Conf. of the IEEE Engineering in Medicine and Biology Society (EMBC)* (2005), pp. 5766–5770.
29. T. A. Stamey, F. S. Freiha, J. E. McNeal, E. A. Redwine, A. S. Whittemore and H. P. Schmid, Localized prostate cancer. relationship of tumor volume to clinical significance for treatment of prostate cancer, *Cancer* **71**(S3) (1993) 933–938.
30. D. Stoianovici, Multi-imager compatible actuation principles in surgical robotics, *Int. J. Med. Robotics Computer Assis. Surg.* **1**(2) (2005) 86–100.

Pedro Moreira joined the University of Twente in 2013 as a Postdoctoral fellow. He obtained his M.Sc. degree in Electrical Engineering from the Federal University of Rio de Janeiro (Brazil). He received his Ph.D. degree in Automatic Systems and Microelectronics from the University of Montpellier (France) in 2012. Before starting his Ph.D., he worked for six years at the Electric Power Research Center in Brazil. His main research interests are surgical robotics, flexible needle steering and control theory.

Gert van de Steeg was born in the Netherlands in 1988. He received the Bachelor degree from the Windesheim University, Zwolle, the Netherlands, in 2010 and his Master degree from the University of Twente, Enschede, the Netherlands, in 2013. He worked at the University of Twente as junior researcher, lab manager and software engineer, since 2013. He has been with the Robotics and Mechatronics research group and currently he is with the Biomechanical Engineering research group. His main areas of research interest are image processing, MRI and ultrasound imaging modalities, algorithm development and medical related research.

Thijs Krabben was born in Winterswijk, the Netherlands, in 1979. He received the B.E. degree in electrical engineering from the Saxion University of Applied Science in Enschede, the Netherlands, in 2004, and the M.Sc. degree in Biomedical Engineering from the University of Twente, Enschede, the Netherlands in 2008. Between 2013 and 2015 he was with Demcon Advanced Mechatronics in Enschede, where he worked as Mechatronic System Engineer at the department of Mechatronic Systems Engineering. His main interests include medical devices including electronics and control systems.

Jonathan Zandman was born in The Netherlands in 1982. He received the B.Sc. degree from Saxion University of Applied Science, Enschede, The Netherlands, in 2007. Since 2011 he has been with Demcon Advanced Mechatronics in Enschede, where he works as senior Industrial Design Engineer at the Department of Mechanical Engineering & Industrial Design.

Edsko Hekman obtained a B.Sc. in Liberal Arts and Engineering at Calvin College (Michigan), and a M.Sc. in Mechanical Engineering at the Delft University of Technology in The Netherlands (1986). After a number of years of developing instrumentation for biomechanical research at the Radboud University (Nijmegen, The Netherlands) he obtained a position at the Biomechanical Engineering group of the University of Twente at the assistant professor level (1993). Research interests are implant technology (e.g., scoliosis correction), prosthetics, rehabilitation and design of medical devices in general.

Ferdinand van der Heijden joined the University of Twente in 1981. He is currently an Associate Professor (UHD) in the Robotics and Mechatronics group within the Faculty of Electrical Engineering, Mathematics, and Computer Science. He is affiliated with MIRA Institute for Biomedical Technology and Technical Medicine. Ferdinand obtained his doctoral degree in the Department of Electrical Engineering at the University of Twente; the Netherlands. Prior to that, he worked for 10 years as an Assistant Professor at the Laboratory for Measurement Science and Instrumentation. Ferdinand is the technical project leader of the project 'Virtual Therapy for Head and Neck Cancer' (www.virtualtherapy.nl), and as such affiliated with the Antoni van Leeuwenhoek Hospital (Netherlands Cancer Institute). He is also the deputy project leader of the EU Horizon project "Murab" (MRI and Ultrasound Robotic Assisted Biopsy, www.murabproject.eu). Ferdinands's broad research interests are primarily in the area of image analysis and surgical navigation. He is also interested in the biomechanical modelling with applications to functional prediction of surgery.

Ronald Borra MD, PhD received his medical training at both the University of Groningen, the Netherlands and the University of Turku, Finland. He obtained his PhD in 2009 at the University of Turku. From 2010 to 2015 he was a post-doctoral Research Fellow at Harvard Medical School, Massachusetts General Hospital – A. A. Martinos Center for Biomedical Imaging, Boston USA. In 2010 he was appointed Adjunct Professor in Experimental Radiology at the University of Turku, Finland and currently works at the University of Groningen. His research has focused on the development of novel MR-derived biomarkers and optimally combining PET and advanced MR methods.

Sarthak Misra joined the University of Twente in 2009. He is currently an Associate Professor in the Department of Biomechanical Engineering within the Faculty of Engineering Technology. He directs the Surgical Robotics Laboratory, and is affiliated with MIRA — Institute for Biomedical Technology and Technical Medicine. He is also affiliated with the Department of Biomedical Engineering, University of Groningen and University Medical Center Groningen. Sarthak obtained his doctoral degree in the Department of Mechanical Engineering at the Johns Hopkins University, Baltimore, USA. Prior to commencing his studies at Johns Hopkins, he worked for three years as a dynamics and controls analyst at MacDonald Dettwiler and Associates on the International Space Station Program. Sarthak received his Master of Engineering degree in Mechanical Engineering from McGill University, Montreal, Canada. He is the recipient of the European Research Council (ERC) Starting grant, Netherlands Organization for Scientific Research (NWO) VENI and VIDI awards, Link Foundation fellowship, McGill Major fellowship, and NASA Space Flight Awareness award. He is the co-chair of the IEEE Robotics and Automation Society Technical Committee on Surgical Robotics, and area co-chair of the IFAC Technical Committee on Biological and Medical Systems. Sarthak's broad research interests are primarily in the area of applied mechanics at both macro and micro scales. He is interested in the modeling and control of electro-mechanical systems with applications to medical robotics.